Check for updates

Cation selectivities in zwitterion grafted nanopores: effect of zwitterion architecture

Kazuya Morishita,[a] Harnoor Singh Sachar, [ID][b] Paul Irving,[a] Nico Marioni,[a] Majid Shahbabaei,[a] Tyler J. Duncan,[a] Zidan Zhang, [ID][a] Ying Zheng,[a] Ashleigh Herrera,[c] Nafiseh Khoshnevisan, [ID][c] Ayse Asatekin [ID][c] and Venkat Ganesan [ID] *[a]

Selective separation of monovalent cations is a critical challenge in applications such as water purification and lithium recovery from salt brines. Cross-linked zwitterionic amphiphilic copolymer (ZAC-X) membranes have gained attention for their exceptional anion permselectivity, attributed to self-assembled zwitterion-lined nanodomains that interact preferentially with anions according to their hydrated radii r_{hyd}. However, these membranes show minimal selectivity among monovalent cations, despite significant differences in their hydration structures, motivating studies on the underlying mechanisms of cation transport and selectivity in this family of materials. In this study, we conducted molecular dynamics simulations of aqueous salt solutions within zwitterion-functionalized nanopores to elucidate the influence of dipole orientation of the zwitterionic (ZI) ligands on cation diffusivities, partitioning, and permeabilities. To this end, we examined two contrasting ZI ligand architectures: Motif A (surface–cation–anion, S–ZI$^+$–ZI$^-$) and Motif B (surface–anion–cation, S–ZI$^-$–ZI$^+$). Our results show that in Motif A, the sulfonate groups of the ZI ligands are localized near the pore center radially, leading to strong electrostatic interactions with small bare cations (Mg^{2+} and Li$^+$). This configuration results in high cation partitioning but low cation diffusion, maintaining solution-diffusion tradeoff typical of functionalized membranes. In contrast, Motif B show that sulfonate groups shift radially toward the mid-region of the pore. This shift, especially for small bare cations, introduces steric constraints that weaken their interactions with the sulfonate groups, thereby enhancing hydration and lowering partitioning, while still maintaining their low self-diffusivity. These findings establish zwitterion dipole orientation as a powerful design lever for tuning cation selectivity in membrane systems and offer molecular-level insights for engineering next-generation ion separation materials.

1 Introduction

Ion separation remains a critical challenge in applications such as water purification, precious metal recovery, and desalination, where precise cation selectivity is essential.[1] Polymer membranes have emerged as promising materials for sustainable separation technologies due to their energy efficiency, cost-effectiveness, and scalability.[2,3] However, conventional polymer membranes typically rely on size-based sieving, charge exclusion, or solution–diffusion mechanisms, which makes it difficult to selectively separate solutes of similar size and charge.[4]

In contrast, biological systems demonstrate exceptional cation selectivity through the interplay of nanoconfinement and solute-specific interactions.[5–7] A well-known example is the potassium channel, which selectively conducts K$^+$ ions *via* precise coordination with carbonyl groups and finely tuned pore dimensions.[8] Inspired by such biological strategies, several studies have developed functionalized polymer membranes that enable reversible and selective interactions with cations by exploiting ion–polymer coordination and specific chemical affinities.[9–11] These systems facilitate the preferential transport of targeted ions over others, thereby enhancing cation selectivity. Nevertheless, the level of selectivity achieved to date remains insufficient for many practical applications.

Zwitterionic (ZI) polymers have recently gained interest as promising candidates for next-generation selective membranes, due to their unique interaction sites provided by zwitterions grafted onto the polymer backbone.[12] Zwitterions feature covalently tethered, oppositely charged groups, which confer

[a] *McKetta Department of Chemical Engineering, The University of Texas at Austin, Austin, TX 78712, USA. E-mail: venkat@che.utexas.edu; Tel: +1 (512) 471-4856*

[b] *Department of Mechanical and Aerospace Engineering, University of Missouri, Columbia, MO 65201, USA*

[c] *Department of Chemical and Biological Engineering, Tufts University, Medford, MA 02155, USA*

distinct properties such as overall charge neutrality, strong hydrophilicity, and large dipole moments.[13] Importantly, these zwitterionic groups offer localized charged interaction sites without invoking the counterion exclusion effects typical of ion-exchange membranes.[14,15]

Numerous studies have reported salt-responsive behavior in ZI polymers, attributed to the complex interplay between zwitterionic moieties and surrounding ions.[13,16,17] Both the identity of the salt ions and the specific chemistry of the zwitterionic groups influence ion distributions and ligand conformations within the polymer matrix. The strength and orientation of the zwitterionic dipole—controlled by the chemical structure and spatial arrangement of the charged groups—play a decisive role in modulating these interactions.[18–20] For instance, Ohno et al. demonstrated that in ZI polymer/salt (Li^+–$TFSI^-$) blends, reversing the zwitterionic dipole orientation significantly impacts ionic conductivity, indicating that dipole orientation can directly influence ion transport pathways.[21,22] Similarly, Jiang and co-workers showed that hydration behavior varies strongly with zwitterion chemistry,[23] and in follow-up work, they demonstrated that increasing the spacing between charged groups —thereby altering dipole strength—substantially impacts antifouling performance.[24] Collectively, these findings suggest that precise molecular engineering of zwitterionic groups provides a viable strategy to tune ion selectivity in polymer membranes.

This study is motivated by the recent work of Lounder et al., who developed highly crosslinked zwitterionic-anion-coordination (ZAC) membranes (X-ZAC) exhibiting unprecedented levels of anion permselectivity, including the highest reported Cl^-/F^- selectivity to date.[14,15] These membranes are fabricated by coating a porous support with a random copolymer of allyl methacrylate (AMA) and sulfobetaine methacrylate (SBMA). The copolymer self-assembles into a bicontinuous network of hydrophilic SBMA-filled nanodomains embedded within a hydrophobic AMA matrix. Subsequent crosslinking regulates the swelling behavior of the hydrophilic domains, yielding effective pore sizes below 1 nm. The scalability, tunability, and exceptional fouling resistance of

this platform make it highly promising for practical separation applications.

In single-salt rejection experiments, X-ZAC membranes exhibit a well-defined trend in monovalent anion selectivity, following the order $I^- > Br^- > Cl^- > F^-$, which inversely correlates with anion hydrated radii r_{hyd}: $I^- \approx Br^- < Cl^- < F^-$.[25] This trend is consistent with stronger interactions between less hydrated, larger anions and the cationic zwitterionic sites, promoting selective partitioning into the membrane. In contrast, while X-ZAC membranes show a clear preference for monovalent over divalent cations—consistent with differences in hydration free energies—they exhibit minimal selectivity among the monovalent cations themselves, despite substantial differences in their hydrated radii r_{hyd}: $Cs^+ < Na^+ < Li^+$.[25] This lack of differentiation suggests that the physical mechanisms underpinning cation transport in zwitterionic membranes are fundamentally different from those governing anion selectivity. In particular, it raises a key question: what are the molecular-level determinants of cation selectivity in zwitterion-functionalized nanochannels?

To address this question, we build upon our earlier work, in which we developed a reduced-order model focused on a single zwitterion-functionalized nanopore confined by a repulsive cylindrical wall.[26,27] This minimalist representation enabled systematic exploration of confinement effects, zwitterion architecture, and ligand density on ion transport at reduced computational cost compared to full bulk simulations. Most recently, we used this model to investigate anion selectivity as a function of zwitterion dipole orientation in nanopores containing sodium halide solutions.[28] Specifically, we compared two zwitterionic configurations: Motif A (surface–cation–anion, S–ZI^+–ZI^-) and Motif B (surface–anion–cation, S–ZI^-–ZI^+) (Fig. 1). Our results showed that anion permeability increased with bare ion radius r_{bare} in both motifs due to stronger interactions between anions and the proximal ZI^+ groups. These interactions localized larger, less hydrated anions near the charged groups, especially in Motif B, where the ZI^+ sites are
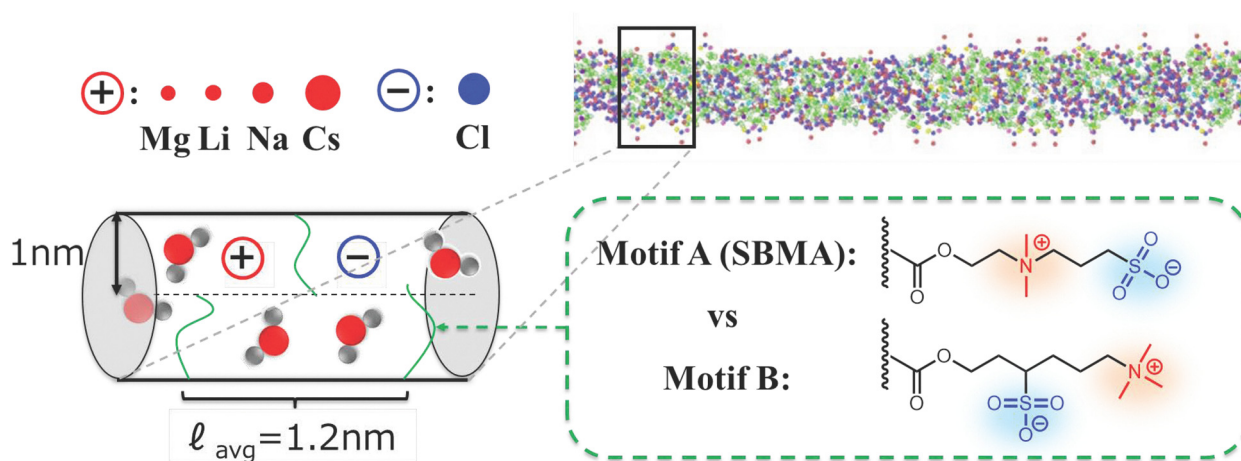

Fig. 1 Schematic representation of a "pore simulation" illustrating a magnified view of the interior of the nanopore, the target structures of zwitterionic ligands, and the target ions of salts for this study.

located near the water-rich pore center. In this configuration, larger anions tend to avoid solvation in the center of the pore and instead maximize favorable interactions with the ZI^+ groups, leading to enhanced partitioning and selectivity. These findings underscored the dominant role of ion partitioning in determining anion permeability in X-ZAC membranes.

Despite the above insights, to the best of our knowledge, no prior study has systematically examined the mechanisms underlying cation solubilities, diffusivities, and overall permeabilities in zwitterion-functionalized nanopores with contrasting dipole orientations. In this work, we address this gap by extending our model framework to investigate the influence of zwitterionic chemistry and dipole orientation on cation transport. This study aims to provide fundamental insights into the molecular design principles required to achieve selective transport among alkali metal cations in zwitterionic membrane systems.

To address this gap, the present study extends our previous computational investigations to examine cation-specific transport behavior and assess the influence of zwitterion (ZI) ligand architecture—specifically, the spatial arrangement of charged groups—on cation selectivity in aqueous salt solutions. We demonstrate that the cation transport properties in zwitterion-functionalized nanopores are governed by electrostatic interactions with the charged groups of the ligands, the surrounding water molecules, and the spatial distribution of both within the pore environment.[28] Building on this insight, we hypothesize that reversing the positions of the charged groups within the SBMA (sulfobetaine methacrylate) zwitterion—i.e., transitioning from Motif A to Motif B—alters the local electrostatic landscape and shifts the spatial distribution of smaller, strongly hydrated cations toward the pore wall due to enhanced interactions with the anionic ZI^- groups. This displacement may increase steric hindrance and lead to distinct partitioning and diffusivity profiles among alkali metal cations.

To test this hypothesis, we performed molecular dynamics simulations of aqueous salt solutions containing different monovalent cations in two nanopore models functionalized with Motif A and Motif B, as defined in our previous study (Fig. 1).[28] We systematically analyzed cation diffusivities, potential of mean force (PMF) profiles, and overall cation permselectivity to quantify the influence of ZI dipole orientation on selective ion transport. These results provide new insights into the molecular-level mechanisms governing cation selectivity in zwitterionic membrane systems.

The rest of this article is organized as follows: in Section 2, we briefly describe the implementation details of the "Model and Force Field," "Reservoir Simulations," "Pore Simulations," and "PMF calculations" to obtain ion diffusivity, partitioning selectivity, and permselectivity. In Section 3, we present our results and discussion: in Section 3.1, we present the partitioning selectivity calculated from PMF profiles within nanopores functionalized with Motifs A and B. In Section 3.2, we present and discuss the differences in ion diffusivities within nanopores between Motifs A and B. In Section 3.3, we estimate the permselectivity calculated based on the partitioning selectivity

and self-diffusivities obtained in Sections 3.1 and 3.2, and compare obtained results with experimental ones. In Section 3.4, we discuss the differences in local interactions and the resulting density distributions of ions within nanopores due to variations in dipole orientation within the ligands, and connect those results to mechanisms explaining the differences in cation partitioning and diffusivities between Motifs A and B. Finally, we summarize our findings and conclusions in Section 4.

2 Simulation details

2.1 Model and force field details

We employed fully atomistic molecular dynamics (MD) simulations to investigate ion transport in zwitterion-functionalized nanopores. Two distinct nanopore models were constructed, each functionalized with zwitterionic ligands exhibiting contrasting dipole orientations: surface–ammonium–sulfonate ($S-ZI^+-ZI^-$, Motif A) and surface-sulfonate–ammonium ($S-ZI^--ZI^+$, Motif B), as illustrated in Fig. 1. In both models, the zwitterionic ligands were grafted from the inner surface of the cylindrical nanopore wall. Simulations were performed on systems containing either water molecules alone (reservoir simulations) or a combination of water molecules and ions (pore simulations and Potential of Mean Force (PMF) Calculations).

To accurately represent the molecular interactions within the zwitterion-functionalized nanopores, we employed the OPLS-AA force field[29,30] for the zwitterionic ligands, the TIP4P/2005 model for water molecules,[31] and the Madrid-2019 and extended Madrid-2019 models for ions.[32,33] Additional details, including force field formulations and parameters, are provided in Section S1 of the SI. All simulations described in this work consistently utilized these force field models.

Transport properties were evaluated using the following protocol. Ion diffusivity was computed through a two-step simulation procedure: reservoir simulations (Section 2.2) followed by pore simulations (Section 2.3). Ion partitioning and permselectivity were similarly assessed through a combination of reservoir simulations and PMF calculations (Section 2.4). To ensure statistical reliability of the computed transport properties, multiple independent initial configurations were generated for each system. In the reservoir and pore simulations, these configurations included varying the spatial arrangement of grafted ZI ligands on the pore surface. For the PMF calculations, however, a fixed grafting pattern was used to isolate the influence of ion–zwitterion interactions from fluctuations in ligand positioning. Each simulation category is described in detail in the following sections.

2.2 Reservoir simulations

The reservoir simulations were designed to model a zwitterion-functionalized nanopore connected to two external reservoirs, each capped by rigid piston particles, as illustrated in Fig. 2. The purpose of this simulation was to determine the overall water density in the pore in equilibrium with the external
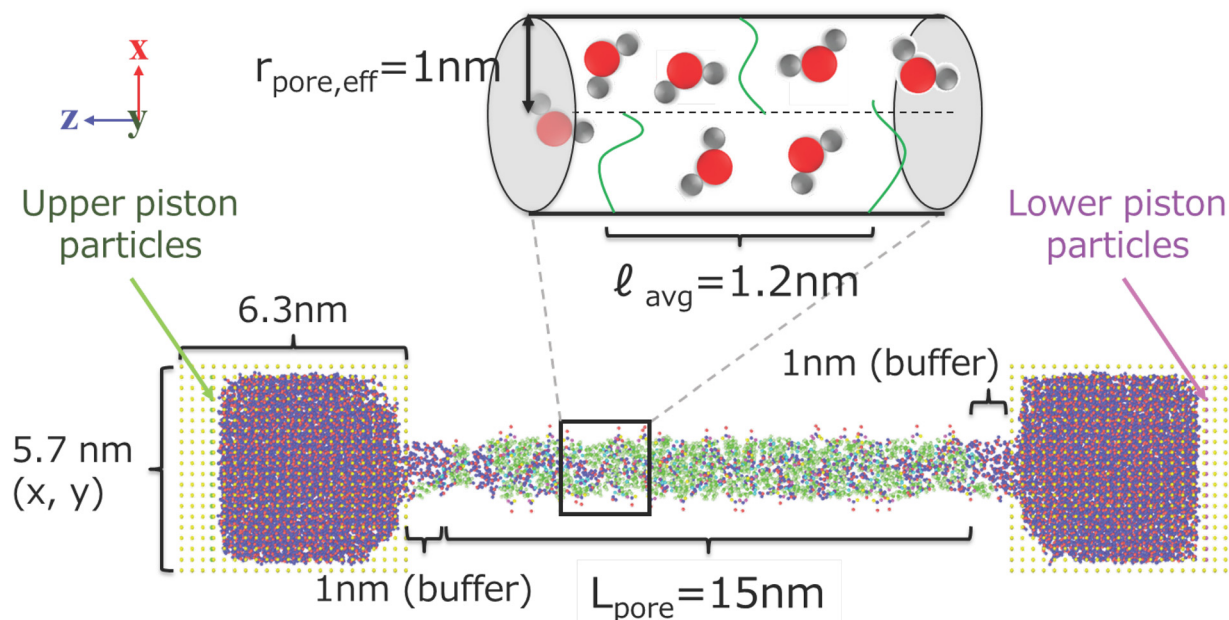
Fig. 2 Schematic representation of a 'reservoir simulation.' A magnified view of the interior of the functionalized nanopore is shown at the top center.

reservoirs. In the initial configuration, the piston particles were fully relaxed along the axial direction of the pore, while the zwitterionic (ZI) ligands were fully extended radially toward the pore center. Both the reservoirs and the nanopore were initially filled with water molecules, without any mobile ions.

The functionalized pore had a fixed axial length of L_{pore} = 15 nm, with 1 nm unfunctionalized buffer zones at each end to mitigate entrance effects between the reservoirs and the functionalized region. The pore radius was set to r_{pore} = 1.2 nm, and the wall thickness was characterized by a Lennard-Jones distance parameter of 0.35 nm. This yields an effective pore radius of $r_{pore,eff} = r_{pore} - 0.35/2 = 1.025$ nm. This value was chosen based on our previous work,[27,28] which successfully reproduced experimental observations. Although this pore radius slightly exceeds the experimentally determined effective pore size of X-ZAC membranes (typically <1 nm),[14,15] the comparison remains valid as the simulations do not account for the steric volume occupied by grafted zwitterionic groups.

The number of ZI ligands grafted to the pore wall (n_{chains}) was chosen to maintain an average separation between adjacent chains of l = 1.2 nm, corresponding to the location of the first nitrogen–nitrogen radial distribution function (RDF) peak observed in prior atomistic simulations of realistic systems ($\sim$0.9–1.0 nm).[26] This value was used to determine the target grafting density σ_g using the relation:

$$l = \frac{1}{\sqrt{\sigma_g}} = \sqrt{\frac{2\pi r_{pore} L_{pore}}{n_{chains}}} \qquad (1)$$

Periodic boundary conditions were applied in the x- and y-directions (perpendicular to the pore axis), while fixed boundary conditions were imposed along the z-axis (pore axis). To minimize Coulombic artifacts from periodic images, the simulation domain included a vacuum region of approximately 12 nm in both lateral directions.

An equal and opposite force was applied to the two pistons to drive water molecules from the reservoirs into the pore under an external pressure of 1 bar. Although experimental filtration conditions often use higher pressures (e.g., 250 psi),[14] such macroscopic pressures are not directly translatable to the nanoscale regime. Instead, this setup was intended to represent equilibrium hydration within zwitterionic nanopores under thermodynamically relevant conditions.

Temperature was maintained at 298.15 K using two separate Nosé–Hoover thermostats, with time constants of 0.2 ps, applied independently to the ZI ligands and water molecules.[34,35] The equations of motion were integrated using a timestep of 2 fs. Equilibration was assessed by monitoring the position of the piston particles and the water number density within the functionalized pore region. Once the water density plateaued, indicating equilibrium, the average number of water molecules in the pore was determined to be $\langle n_A \rangle$ = 498 for Motif A and $\langle n_B \rangle$ = 339 for Motif B. These densities were subsequently used as inputs for the pore simulations, while the corresponding equilibrated configurations were used for the PMF calculations described below.

2.3 Pore simulations

The initial configuration for the pore simulations consisted solely of the zwitterion-functionalized nanopore, corresponding to the functionalized region in the reservoir simulations, as shown in Fig. 1. To probe ion transport within the nanopores, salt ion pairs (either alkali or alkaline earth chlorides) were introduced to achieve an approximate concentration of 1 M, based on the calculated pore volume. In actual polymer membrane nanopores, a macroscopic concentration gradient

develops from the feed side to the permeate side. However, reproducing such a gradient in all-atom molecular dynamics simulations is challenging. Therefore, the simulation setup was intended to represent the equilibrium salt concentration within zwitterionic nanopores under thermodynamically relevant conditions. Considering that the feed concentration of a salt solution in experimental systems (*e.g.*, 20 mM)[14] is generally enriched within nanopores, and in order to obtain statistically significant data on ion transport, a uniform 1 M salt solution was selected.

To maintain a constant internal pressure of 1 bar, an equal number of water molecules was removed from the system to compensate for the addition of ions, using the average water occupancy determined in the reservoir simulations (Section 2.2). The number of salt pairs (n_{salts} = 30) was selected to ensure statistically meaningful sampling of ion transport behavior.

The ZI ligands in the initial structure were fully extended radially toward the center of the pore. The same parameters for pore length (L_{pore}), effective pore radius ($r_{pore,eff}$), and inter-chain spacing (l) used in the reservoir simulations were also adopted here. Periodic boundary conditions were applied in all spatial directions. To minimize spurious electrostatic interactions due to periodicity, a vacuum region of approximately 12 nm was included in directions perpendicular to the pore axis.

Each system was equilibrated under the NVT ensemble for approximately 20 ns, followed by a production run of 200 ns in the same ensemble. Nosé–Hoover thermostats with a time constant of 0.2 ps were applied to the water molecules, ions, and ZI ligands to maintain a constant temperature of 298.15 K.[34,35] A timestep of 2.0 fs was used to integrate the equations of motion.

Ion self-diffusion coefficients (D_{ion}) were computed from the slope of the long-time mean-squared displacement (MSD) along the pore axis, according to the following expression:[36]

$$D_{ion} = \lim_{t \to \infty} \frac{1}{2} \frac{d\text{MSD}_{ion,axial}(t)}{dt} \qquad (2)$$

The MSD derivative was calculated over a 50 ns window where the MSD followed diffusive scaling, with a log–log slope of $m = 1 \pm 0.02$ with $R^2 \geq 0.998$. MSD data were averaged over four independent 200 ns trajectories to identify the appropriate linear regime for diffusion analysis.

2.4 Potential mean force (PMF) calculations

To compute the potential of mean force (PMF) profiles along the axial direction of the nanopore, we used the fully equilibrated configuration obtained from the reservoir simulations. The reaction coordinate, z, corresponding to the pore axis, was divided into 106 windows of width 2 Å each, spanning from $z = -30$ Å to $z = 180$ Å. For each window, a cation was placed at the center (starting from $z = -30$ Å), resulting in 106 independent umbrella sampling simulations. Any water molecules overlapping with the inserted cation were removed to avoid steric clashes and to stabilize the initial configuration.

A harmonic biasing potential was applied along the z-axis to restrain the cation to the center of its designated window, using a spring constant of 0.1 kcal mol^{-1} Å^{-2}. To confine the cation radially within the pore when positioned near the reservoir regions, we employed a flat-bottom restraining potential $u(x, y)$, as proposed by Zhu and Hummer:[37]

$$u(x, y) = \begin{cases} 0 & \text{if } x^2 + y^2 < R^2 \\ \frac{1}{2}K\left[\sqrt{x^2 + y^2} - R\right]^2 & \text{if } x^2 + y^2 \geq R^2 \end{cases} \qquad (3)$$

where x and y are coordinates in directions perpendicular to the pore axis (Fig. 2), $R = r_{pore} = 1.2$ nm is the geometric pore radius, and $K = 10$ kcal mol^{-1} Å^{-2} is the spring constant of the restraining potential.

Each umbrella sampling simulation was preceded by a 1 ns equilibration period, followed by a 2 ns production run. Cation coordinates were recorded every 20 fs during the production phase. All other simulation parameters—including thermostat type and settings, boundary conditions, pressure regulation *via* pistons, and timestep—were identical to those employed in the reservoir simulations (Section 2.2).

The cation trajectories collected from the umbrella sampling simulations were analyzed using the Weighted Histogram Analysis Method (WHAM),[38] implemented *via* the WHAM software package developed by the Grossfield Lab.[39,40] For each zwitterion-functionalized nanopore system, four independent sets of umbrella sampling simulations were conducted by varying the initial cation insertion coordinates slightly. The final PMF profile was obtained by averaging over these four replicates to ensure statistical robustness.

Using the averaged PMF profiles, cation permeability ratios (permselectivity) were calculated according to the following expression:[37]

$$\frac{P_m}{P_n} = \frac{\int_{z_{begin}}^{z_{end}} \frac{\exp\left[\frac{F_n(z)}{k_B T}\right]}{D_n(z)} dz}{\int_{z_{begin}}^{z_{end}} \frac{\exp\left[\frac{F_m(z)}{k_B T}\right]}{D_m(z)} dz} \qquad (4)$$

where P_m and P_n denote the permeabilities of cations m and n (with m, n = Mg^{2+}, Li$^+$, Na$^+$, or Cs$^+$), $F_m(z)$ and $F_n(z)$ are the corresponding PMF profiles, and $D_m(z)$ and $D_n(z)$ are the local self-diffusivity coefficients. Due to the large statistical uncertainty associated with estimating $D(z)$ from umbrella sampling data, we instead used the average self-diffusivity values obtained from the pore simulations and assumed these values to be uniform along the pore axis.

Finally, the ratio of cation partition coefficients (partition selectivity) was derived by combining eqn (4) with the solution-diffusion model,[41–44] $P_i = K_i \times D_i$, where K_i is the partition

coefficient and D_i is the diffusivity of ion i. This yields the expression:

$$\frac{K_m}{K_n} = \frac{\int_{z_{begin}}^{z_{end}} \exp\left[\frac{F_n(z)}{k_B T}\right] \mathrm{d}z}{\int_{z_{begin}}^{z_{end}} \exp\left[\frac{F_m(z)}{k_B T}\right] \mathrm{d}z} \tag{5}$$

where K_m and K_n represent the partition coefficients for cations m and n, respectively (m, n = Mg^{2+}, Li^+, Na^+, or Cs^+ in our simulations).

3 Results and discussion

We investigated the ion transport behavior of various cation chlorides in aqueous solutions through two distinct nanopores functionalized with zwitterionic ligands arranged in contrasting configurations, referred to as Motifs A and B (Fig. 1). Motif A corresponds to the SBMA ligand commonly used in X-ZAC membranes, featuring a surface-exposed ammonium-sulfonate configuration. In contrast, Motif B consists of the same charged groups arranged in reverse order: the sulfonate group is tethered as a side chain to a carbon backbone, placing the quaternary ammonium group at the flexible terminus of the ligand, resulting in a surface-sulfonate-ammonium configuration. While Motif B has not been experimentally realized in membrane architectures, its comparison with Motif A enables us to isolate and evaluate the impact of charged group spatial arrangement on cation density distributions and steric exclusion-driven selectivity within the pore.

The cations selected for this study—Mg^{2+}, Li^+, Na^+, and Cs^+—span both alkali and alkaline earth metals and are commonly reported in the experimental literature.[14] These ions vary not only in valence, with Mg^{2+} being divalent and the others monovalent, but also in bare ionic radius r_{bare} and charge density. Table 1 summarizes their key physical properties. Notably, Mg^{2+} exhibits the highest charge density and hydration free energy, along with the largest hydrated radius r_{hyd}, consistent with its small bare ionic radius r_{bare} and strong electrostatic interactions with water molecules. Among the monovalent cations, hydration free energy and hydrated radius r_{hyd} decrease in the order: Li^+ > Na^+ > Cs^+, reflecting trends in bare ionic radius r_{bare} and charge density. Throughout this study, we refer to the bare ionic radius r_{bare} when discussing ion size, unless otherwise specified. This simplifies the discussion and avoids conflation with the hydrated radius r_{hyd}.

Simulations were conducted at a bulk salt concentration of approximately 1 M to simplify the representation of the system within the pore, as described in Section 2.3. The nanopore radius was fixed at 1.025 nm, and the average separation between zwitterionic ligands was set to 1.2 nm to ensure consistent pore geometry. The selected radius of 1.025 nm approximates experimentally relevant conditions, and the ligand spacing of 1.2 nm reflects the spacing observed in simulation snapshots representative of realistic grafting densities,[26] as discussed in Section 2.2.

3.1 Potential of mean force profiles and partitioning selectivity

Fig. 3 displays the potential of mean force (PMF) profiles obtained using the methodology described in Section 2.4, along with the 95% confidence intervals (shaded regions). The reaction coordinate, z, spans from the interior of one reservoir ($z = -30$ Å) to that of the other ($z = 180$ Å), traversing the entire pore region (-10 Å $< z <$ 160 Å). We approximated the environment surrounding a cation within the reservoir as equivalent to that in bulk water, assuming it represents the
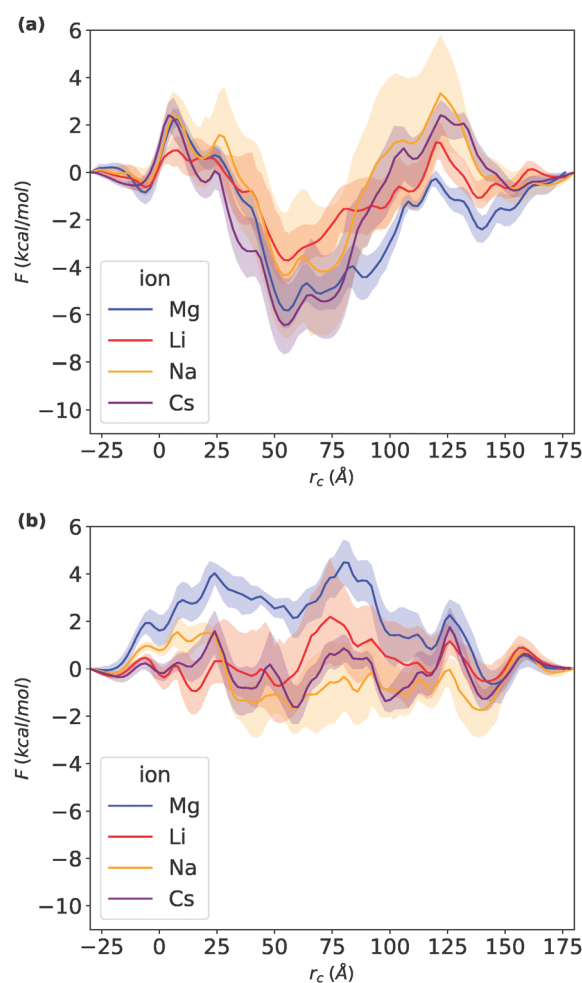

Fig. 3 PMF profiles for various cations in nanopores functionalized with (a) ligand Motif A and (b) ligand Motif B.

Table 1 Ionic radii, hydration radii, and hydration free energies of selected cations

Cation	Ionic radius r_{bare} (Å)	Hydrated radius r_{hyd} (Å)[a]	Hydration free energy (kJ mol^{-1})[b]
Mg^{2+}	0.65	4.28	1830
Li^+	0.60	3.82	475
Na^+	0.95	3.58	365
Cs^+	1.69	3.29	250

[a] Hydrated radii from ref. 25. [b] Hydration free energies from ref. 45.

region sufficiently distant from the pore entrance. In such regions, cation interactions with the zwitterion-functionalized pore are negligible. Under this assumption, we normalized the PMF values for each cation species at positions $z = -30$ Å and $z = 180$ Å to zero, providing a baseline for PMF comparison among the different cation species.

As shown in Fig. 3, the potential of mean force (PMF) profiles for cations exhibit consistent qualitative features within a given ligand motif. Specifically, both motifs display axial profiles characterized by local maxima and minima, which arise from the non-uniform, random spatial distribution of the 79 zwitterionic ligands along the inner pore wall. This heterogeneity breaks axial symmetry and leads to spatial variations in the local electrostatic and steric environment. Fig. S2 in the SI presents the axial profiles of the number ratios of water molecules to the sulfonate and ammonium groups of ZI ligands, N_{H_2O}/N_{ZI-FGs}, along with the corresponding PMF profiles. This comparison shows that local PMF maxima coincide with regions of reduced water density or elevated ligand volume fraction (e.g. minima of N_{H_2O}/N_{ZI-FGs} profiles), whereas PMF minima align with maxima of N_{H_2O}/N_{ZI-FGs} profiles, highlighting the coupling between solvent distribution and ion energetics.

A key difference emerges when comparing Motifs A and B. Motif A exhibits a pronounced PMF minimum near the pore center, indicating a region of enhanced ion stabilization, likely due to favorable solvation and balanced electrostatic interactions. In contrast, Motif B produces flatter PMF profiles along the axial direction, suggesting a more diffuse and less structured electrostatic environment, which may limit strong localization of cations.

Furthermore, the magnitude and spatial distribution of PMF barriers differ substantially across cation species for both motifs, reflecting the interplay of bare cation size (e.g. r_{bare}), hydration energetics, and interaction strength with zwitterionic groups. These variations underscore the importance of zwitterion dipole orientation in modulating the free energy landscape experienced by ions within the nanopore.

To quantify cation partitioning selectivity, we employed the approach proposed by Zhu and Hummer,[37] in which partitioning is determined from the axial potential of mean force (PMF). The resulting partitioning values, normalized relative to that of Li^{+}, are shown in Fig. 4 and listed in Table S9 of the SI. As seen in Fig. 4(a), the simulated partitioning selectivity for Motif A shows good agreement with experimental trends, supporting the validity of our modeling approach. A slight overestimation is observed for Cs^{+}, but the overall trend is well captured.

A key insight emerges by comparing Fig. 4(b) and 3, which reveals an inverse relationship between the height of PMF energy barriers and ion partitioning. In Motif A, Li^{+} exhibits the highest partitioning, followed by Mg^{2+}, with Na^{+} and Cs^{+} showing significantly lower values. This hierarchy directly correlates with the energy landscapes shown in Fig. 3(a). Specifically, Li^{+} experiences relatively low energy barriers in the interfacial regions of the pore, which correspond to approximately 0 Å < z < 20 Å and 100 Å < z < 150 Å. These axial
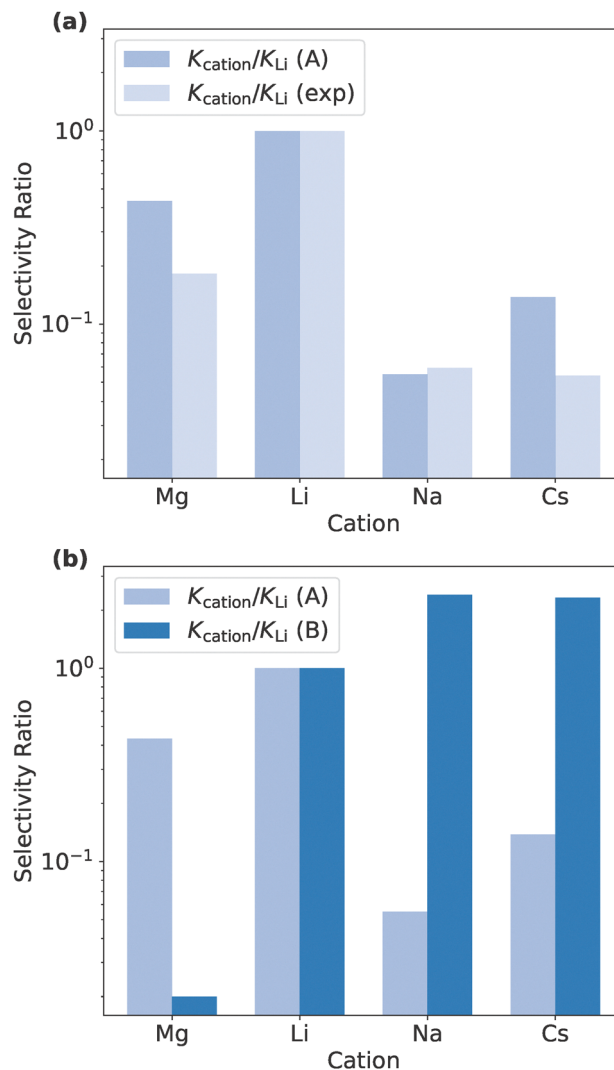

Fig. 4 Partitioning selectivity of various cations with respect to Li^{+} in nanopores functionalized with Motifs A and B. (a) Comparison between simulation results for Motif A and experimental results (see Table S10 in the SI). (b) Comparison of simulation results between Motifs A and B.

regions contain segments where the average ratio N_{H_2O}/N_{ZI-FGs} is less than four (see: Fig. S2(a) in the SI), representing water-poor (ZI-rich) regions. In contrast, Mg^{2+} encounters a high barrier in the first interfacial region but a low one in the second, resulting in moderate overall partitioning. Na^{+} and Cs^{+} face substantial energy barriers in both regions, leading to diminished partitioning. Interestingly, although some ions exhibit deep PMF minima near the pore center (roughly 20 Å < z < 100 Å), these central minima do not contribute significantly to partitioning.

For Motif B, the selectivity trend is reversed: Na^{+} and Cs^{+} exhibit higher partitioning than Li^{+} and Mg^{2+}, with Mg^{2+} showing the lowest value. As shown in Fig. 3(b), Mg^{2+} experiences the highest PMF barriers throughout the pore length. Among monovalent cations, Li^{+} experiences elevated energy barriers near the intermediate region (60 Å < z < 100 Å), reducing its partitioning efficiency relative to Na^{+} and Cs^{+}.

Fig. S2(b) of the SI shows that, while the region with $N_{H_2O}/N_{ZI-FGs} < 4$ (water-poor) spans most of the pore region in Motif B, Li$^+$ experiences a severely water-depleted environment in this intermediate region, where N_{H_2O}/N_{ZI-FGs} approaches one.

In summary, cation partitioning behavior is seen to be highly sensitive to ligand architecture. In Motif A, Li$^+$ and Mg^{2+} ions partition most effectively, a trend governed by energy barriers in the regions containing segments where $N_{H_2O}/N_{ZI-FGs} < 4$ (water-poor or ZI-rich). Conversely, in Motif B, Na$^+$ and Cs$^+$ dominate, with partitioning determined by cumulative energy barriers distributed across the entire pore. These results underscore the critical role of ligand spatial configuration in tuning ion selectivity *via* steric and electrostatic interactions.

3.2 Ion diffusivities

Fig. 5 shows the ion self-diffusivities of magnesium chloride and various alkali chlorides within nanopores functionalized with Motifs A and B. Although the absolute diffusivities in Motif B are consistently lower than those in Motif A, both ligand environments exhibit the same general trend: ion diffusivity increases with the bare cation radius r_{bare}. This behavior mirrors that observed in unfunctionalized pores (Fig. S3 in the SI) and aligns with experimentally established trends for cation

(a)

(b)

Fig. 5 Comparison of ion self-diffusivities for various cation chlorides in the functionalized nanopores between (a) Motif A and (b) Motif B.

diffusivity in salt-in-water systems. Notably, the simulated diffusivity of Na$^+$ within the SBMA-functionalized nanopore $(6.38 \times 10^{-8} \text{ cm}^2 \text{ s}^{-1})$ agrees well with experimental values for NaCl solutions in X-ZAC membranes [$(4.89-6.59) \times 10^{-8} \text{ cm}^2 \text{ s}^{-1}$, depending on feed concentration],[14] validating that our simulation framework captures the essential ion-zwitterion dynamics at relevant timescales within functionalized nanodomains of X-ZAC membranes.

The relative ordering of cation and anion diffusivities, however, diverges markedly between the two ligand motifs. In Motif A, the diffusivities of Mg^{2+} and Li$^+$ are lower than that of Cl$^-$, whereas Na$^+$ and Cs$^+$ diffuse faster than Cl$^-$. By contrast, in Motif B, all cation diffusivities fall below that of Cl$^-$, indicating substantial differences in the electrostatic and steric environments experienced by the ions in the two motifs. These contrasting behaviors are discussed in greater detail in Section 3.4.

In summary, both ligand motifs yield a consistent trend of increasing cation diffusivity with bare ionic radius r_{bare}. However, Motif B systematically exhibits reduced ion mobility compared to Motif A, and the cation–anion diffusivity hierarchy is highly motif-dependent.

3.3 Permselectivity

The partitioning and diffusivity behaviors of various cations were discussed in Sections 3.1 and 3.2. Building upon these results, cation permselectivity was estimated using the solution–diffusion framework outlined in Section 2.4. This approach enables direct comparison between simulated and experimental selectivity for Motif A and provides predictive insights into cation permselectivity for Motif B.

Fig. 6 shows the simulated cation permeability values, normalized by that of Li$^+$, for nanopores functionalized with Motifs A and B. In Fig. 6(a), corresponding experimental permselectivity values were derived from rejection data for cation chlorides, following the procedure described in the SI (Section S2).[46] Comparison of these experimental data with the simulation results for Motif A (Fig. 6(a)) reveals good agreement in the overall selectivity trend. In particular, the permeabilities of Li$^+$, Na$^+$, and Cs$^+$ are comparable, while Mg^{2+} exhibits significantly lower permeability. Although the simulated permselectivity of Cs$^+$ is slightly overestimated, the general trend remains consistent with experimental observations.

The almost comparable permeabilities for monovalent cations in Motif A can be attributed to a partitioning–diffusivity trade-off commonly observed in functionalized polymer membranes.[47–49] As discussed in Sections 3.1 and 3.2, in Motif A, the partitioning coefficient decreases with increasing bare cation radius r_{bare} (*e.g.*, from Li$^+$ to Cs$^+$), whereas diffusivity increases. In contrast, Mg^{2+} exhibits both the lowest partitioning and diffusivity, consistent with its high charge density, which strongly suppresses its permeability relative to the monovalent cations.

In Motif B, the permselectivity trends deviate substantially from those in Motif A. Specifically, the Na$^+$ and Cs$^+$ ions exhibit significantly higher permselectivity relative to Li$^+$, indicating enhanced separation of these ions in the Motif B-functionalized
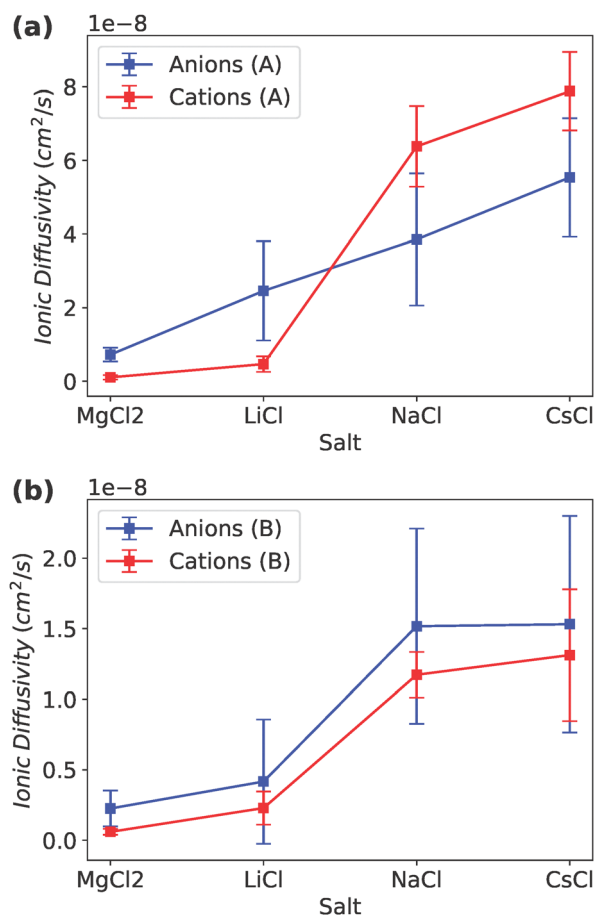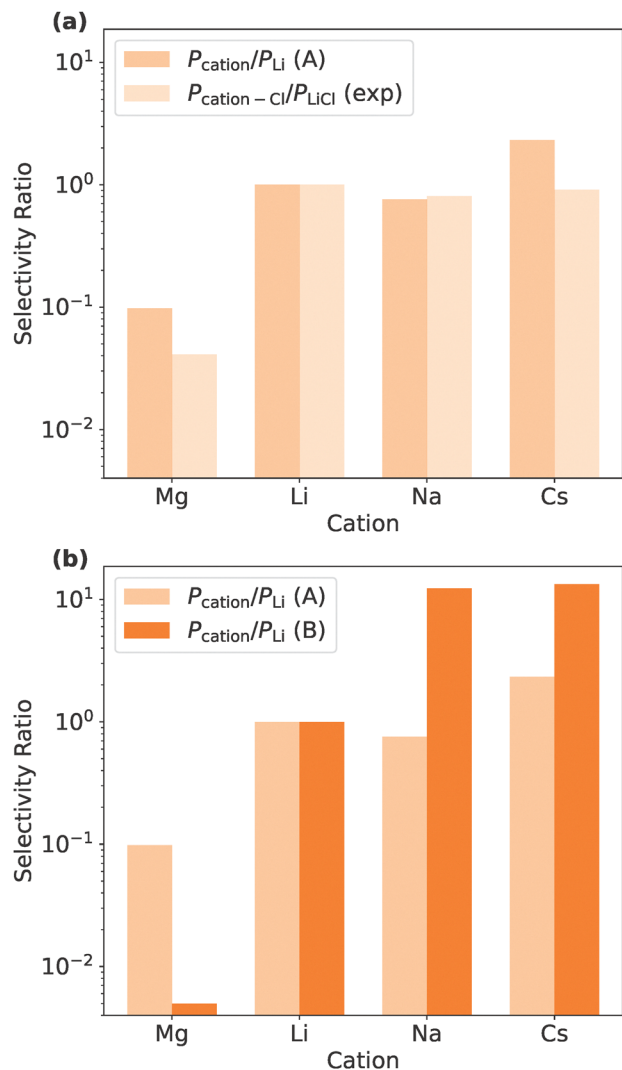
Fig. 6 Permselectivity of various cations with respect to Li$^+$ in nanopores functionalized with Motifs A and B. (a) Comparison between simulation results for Motif A and experimental results (see Table S8 in the SI). (b) Comparison of simulation results between Motifs A and B.

pore. Although the diffusivity trends remain similar between Motifs A and B, the partitioning behavior differs notably [Fig. 4(b)]. In Motif B, the relative partitioning of Na$^+$ and Cs$^+$ with respect to Li$^+$ is higher than in Motif A (Section 3.1), primarily due to the pronounced reduction in Li$^+$ partitioning while its diffusivity remains low. This shift effectively disrupts the typical partitioning–diffusivity trade-off. Additionally, Mg^{2+} shows even lower permeability in Motif B, driven by further suppression of its partitioning. These observations suggest that Motif B-functionalized nanopores exhibit significantly enhanced permselectivity for Na$^+$ and Cs$^+$ over Li$^+$, and stronger selectivity for monovalent cations over Mg^{2+} compared to Motif A.

Beyond the changes in partitioning selectivity, the observed differences in permselectivity between the two motifs reflect a broader permeability–selectivity trade-off, a hallmark of many membrane systems.[41,50] Fig. S4 in the SI illustrates this

relationship *via* log–log plots of permeability *versus* permselectivity for both motifs. In Motif A, which supports higher overall permeability, the selectivity remains relatively unchanged across the cation series from Li$^+$ to Cs$^+$. This suggests that ion transport is facilitated at the expense of discrimination between cations, likely due to lower energy barriers. In contrast, Motif B exhibits lower overall permeability but a more pronounced increase in selectivity across the same series, indicating stronger ion discrimination as a result of higher transport energy barriers. This contrast in permeability–selectivity behavior further highlights the distinct ion transport characteristics imparted by the two ligand environments.

To summarize, the simulated permselectivity trends for Motif A agree well with experimental data, reinforcing that ion partitioning is the dominant factor governing cation permeability in this system. For Motif B, reversing the charge arrangement in the SBMA ligands leads to significantly reduced partitioning for both Li$^+$ and Mg^{2+}, with a more severe reduction for Mg^{2+} than for Na$^+$ or Cs$^+$. As a result, nanoporous membranes functionalized with Motif B are predicted to display markedly higher permselectivity for Na$^+$ and Cs$^+$ over Li$^+$, and substantially improved selectivity of monovalent cations over Mg^{2+}, compared to current X-ZAC membrane designs.

3.4 Local interactions and distribution profiles

In this section, we first examine the differences in local ion interactions (Section 3.4.1) and spatial ion density distributions (Section 3.4.2) between Motifs A and B. Building on these observations, we then analyze the implications for cation permselectivity and ion self-diffusivities (Section 3.4.3), linking these interaction-level differences to the transport behaviors discussed in Sections 3.1 and 3.2 for each motif.

3.4.1 Differences in ion interactions. To gain molecular-level insights into the cation partitioning and diffusivity trends described in Sections 3.1 and 3.2, we analyzed the electrostatic interactions between cations and oppositely charged species in the functionalized nanopores. Specifically, we computed radial distribution functions (RDFs) between cations and sulfonate oxygens (O$_s$), cations and water oxygens (O$_w$) (Fig. 7), and cations and chloride ions (Cl$^-$) [Fig. S5(c), SI] in both Motif A and Motif B.

For Motif A, the RDFs indicate that cation–O$_s$ and cation–O$_w$ interaction strengths decrease with increasing bare cation radius r_{bare}. Notably, Na$^+$ and Cs$^+$ show stronger interactions with water oxygens than with sulfonate groups, whereas Li$^+$ and Mg^{2+} exhibit stronger coordination with sulfonate oxygens than with water molecules, suggesting their stronger electrostatic affinity to the charged ligands.

In Motif B, although the overall size-dependent trend in RDF intensities remains similar to Motif A, there is a qualitative change in the relative strengths of cation–ligand and cation–solvent interactions, especially for Li$^+$ and Mg^{2+}. Both ions show significantly weaker interactions with sulfonate groups and stronger coordination with water molecules compared to their behavior in Motif A. For Na$^+$ and Cs$^+$, the cation–O$_s$ interaction strengths remain largely unchanged across motifs,
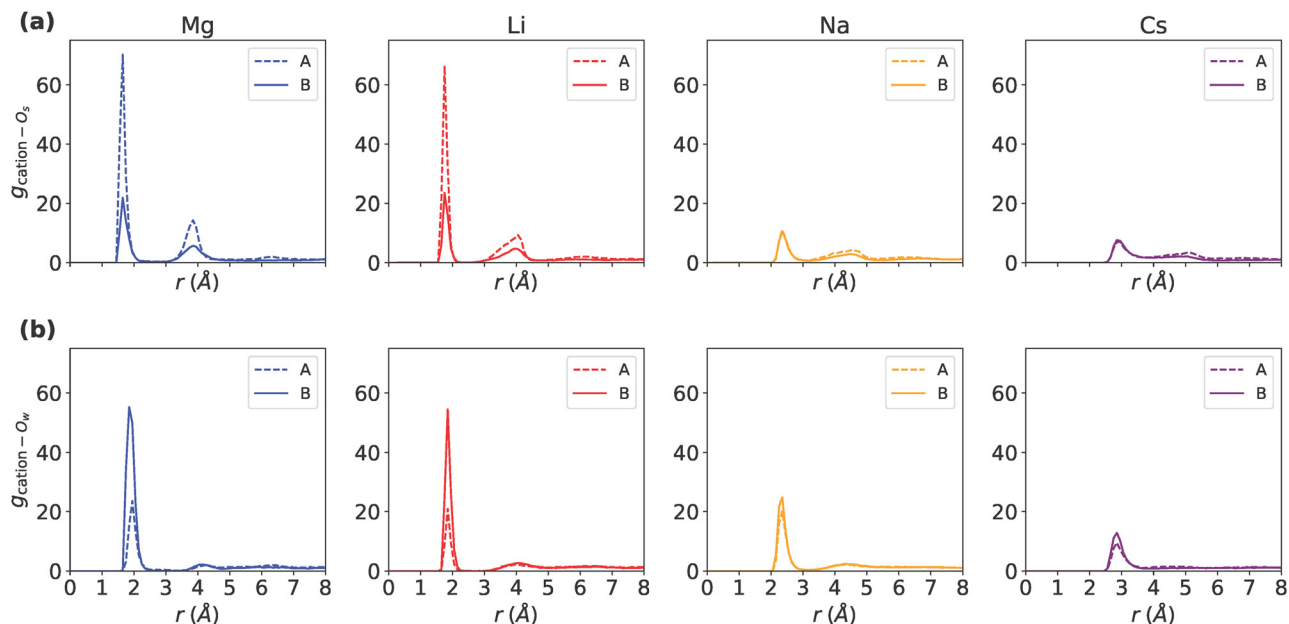
Fig. 7 RDFs for various cation chlorides (a) between cation and sulfonate oxygen (O_s) and (b) between cation and water oxygen (O_w).

while cation–O_w interactions are enhanced in Motif B, indicating an overall shift toward solvation-dominated coordination.

RDFs for cation–Cl^- interactions [Fig. S5(c), SI] reveal that strong ion pairing occurs predominantly for Na^+ in Motif B. To complement the cation interaction analysis, we also examined RDFs for Cl^- interactions with ammonium nitrogens (N) and water oxygens (O_w), shown in Fig. S5(a) and (b) of the SI, respectively. These results indicate that Cl^- ions exhibit generally higher RDF intensities in Motif B than in Motif A, suggesting that Motif B promotes closer association of

anions with both the functional groups and the hydration environment.

3.4.2 Differences in ion density distributions. To understand the differences in electrostatic interactions observed between Motifs A and B, we analyzed the radial number density profiles of various ions within the functionalized nanopores (Fig. 8).

In Motif A, the radial density profiles of water [Fig. S6(a), SI] exhibit a pronounced peak at the center of the pore, with intensity decreasing monotonically toward the pore wall across
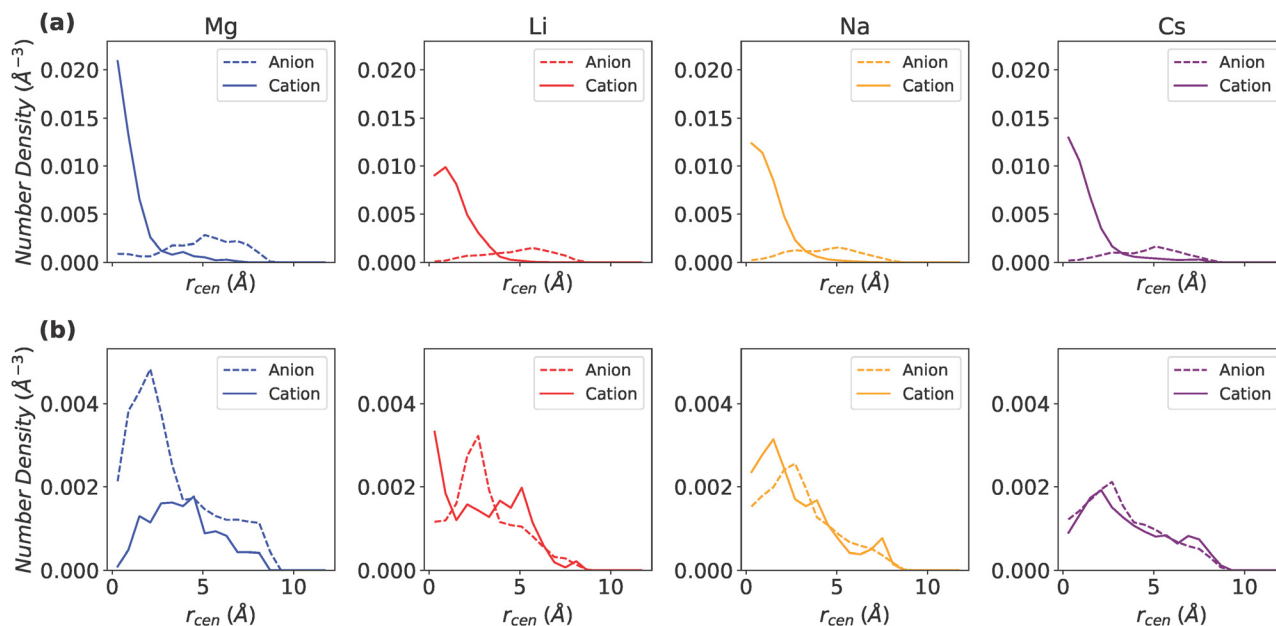

Fig. 8 Radial profiles of the number density of cations and anions for various cation chlorides within nanopores functionalized by (a) Motif A and (b) Motif B.

all cation systems. This spatial distribution of water molecules correlates strongly with the observed cation densities in Fig. 8(a), where all cations preferentially localize near the pore center, consistent with their tendency to occupy the water-rich region. Among the cations examined, Mg^{2+} shows the highest central density, reflecting its strong hydration preference and affinity for polar environments.

A more detailed analysis reveals that, for the Mg^{2+} system, approximately twice as many Cl^- counterions accumulate at intermediate radial positions—between the pore center and wall—relative to systems containing monovalent cations. This accumulation is driven by electrostatic interactions between Cl^- and the positively charged quaternary ammonium groups tethered to the zwitterionic ligands [Fig. S5(a), SI]. The local excess of Cl^- ions, in turn, induces strong electrostatic repulsion with nearby sulfonate groups, leading to a redistribution of the zwitterionic ligands and an elevated sulfur density near the pore center [Fig. S7(a), SI]. This electrostatically restructured environment reinforces the central localization of Mg^{2+} ions, which possess a high affinity for sulfonate groups.

Among the monovalent cations, the position of the density peak in Motif A shifts progressively toward the center as bare ionic radius r_{bare} increases from Li^+ to Cs^+. This trend reflects a balance between cation–sulfonate interactions and hydration preferences. Li^+, which strongly coordinates with sulfonate groups, exhibits a density peak slightly off-center that overlaps with the sulfur-rich region [Fig. 7(a)]. In contrast, Na^+ and Cs^+ preferentially localize closer to the pore center, suggesting a dominant preference for solvation by water molecules rather than sulfonate coordination [Fig. 7(a) and (b)]. Correspondingly, the first peak in the sulfur density shifts outward from the center as bare cation radius r_{bare} increases [Fig. S7(a), SI], consistent with the weakening of cation–sulfonate interactions along the series.

In Motif B, the water density profiles [Fig. S6(b), SI] exhibit a slight shift of the peak towards the pore wall relative to Motif A, although the overall shape of the profile remains similar across all cation species. Correspondingly, the cation density profiles shift away from the pore center [Fig. 8(b)], following the relocation of sulfonate groups to intermediate radial regions between the center and the wall [Fig. S7(b), SI]. Notably, Mg^{2+} and Li^+—which exhibit strong interactions with sulfonate groups in Motif A—are now primarily distributed in this intermediate region, corresponding to the zwitterion-rich (ZI-rich) zone [Fig. S8(b), SI]. However, steric constraints imposed by the zwitterionic ligands in this region hinder effective coordination with sulfonate groups. As a result, these cations exhibit comparatively stronger interactions with water molecules [Fig. 7(b)] than in Motif A. In contrast, the spatial distributions of Na^+ and Cs^+—which intrinsically interact weakly with sulfonate groups due to their low charge densities—are relatively insensitive to the shift in sulfonate position.

Across all cation chloride systems, Cl^- ions shift toward the pore center in Motif B, where they interact more closely with centrally localized quaternary ammonium groups [Fig. S9(b), SI]. This shift leads to increased spatial overlap between cation and

anion density profiles in Motif B compared to Motif A. Such overlap is consistent with the stronger ion pairing observed for Na^+ and Cl^- in Motif B. Furthermore, the pore center in Motif B is characterized by a high water density and reduced steric hindrance [Fig. S6(b) and S8(b), SI], providing an environment that facilitates stronger electrostatic interactions between Cl^- ions, ammonium groups, and surrounding water molecules [Fig. S5(a) and (b), SI].

Taken together, these results highlight how zwitterion dipole orientation can reorganize the spatial positioning of sulfonate and ammonium groups, reshaping the electrostatic and steric landscape of the nanopore. This reorganization, in turn, modulates the balance between ion–ligand and ion–solvent interactions, leading to significant changes in cation and anion localization. These structural effects play a central role in determining partitioning behavior and selectivity in zwitterionic membranes.

3.4.3 Mechanisms underlying cation transport properties. The trends observed in cation partitioning selectivity and self-diffusivities, discussed in Sections 3.1 and 3.2, reflect the above differences in electrostatic interactions and the spatial distribution of ions. Explicitly, we propose that the cation partitioning in Motif A is determined by the competition between the water coordination and sulfonate coordination for the cation. In contrast, cation diffusivity, since it reflects only partitioned ions, is expected to only be influenced by its slowing arising from the electrostatic interactions with the sulfonate groups.

To validate the above hypotheses, Fig. 9 shows the ratio of the coordination number between cations and sulfonate oxygen (O_s) to the total oxygen coordination (including both sulfonate and water oxygen, O_{total}). This ratio provides a quantitative measure of the extent to which cations prefer sulfonate coordination over hydration within each ligand motif. In Motif A, this ratio is highest for Li^+ and Mg^{2+}, with Li^+ slightly exceeding
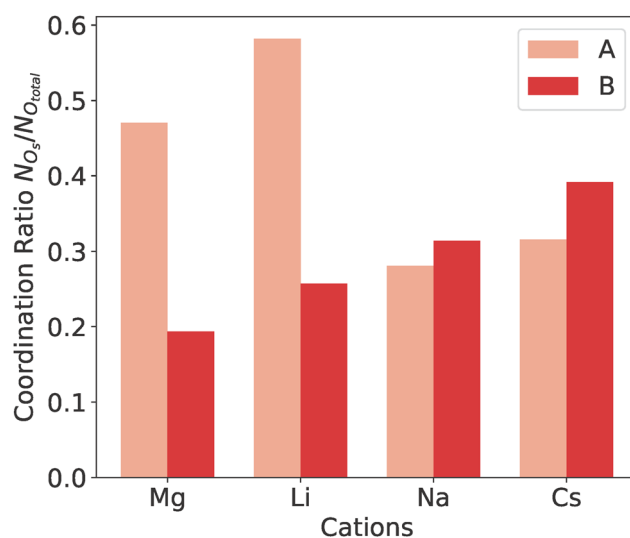

Fig. 9 Ratio of coordination numbers between cation–O_s and cation–O_{total} combinations in nanopores functionalized with Motifs A and B from pore simulations.

Mg^{2+}, indicating strong cation–sulfonate interactions. In contrast, Na^+ and Cs^+ exhibit substantially lower coordination ratios, with Cs^+ marginally higher than Na^+. These trends correlate with the partitioning selectivity observed in Fig. 4, supporting the conclusion that higher sulfonate coordination—facilitated by partial dehydration—promotes increased partitioning in Motif A.

Regarding ion diffusivities in Motif A, the decreasing intensities in both cation–O_s and cation–O_w RDFs with increasing bare cation radius r_{bare} (Fig. 7) suggest that lower charge densities lead to weaker electrostatic interactions with oxygen atoms. This weakening of interactions results in enhanced cation diffusivity. Notably, only Mg^{2+} and Li^+ exhibit strong electrostatic interactions with sulfonate groups at the pore center in Motif A [Fig. 7(a)], which explains pronounced reduction in their mobility relative to Na^+ and Cs^+ [Fig. 5(a)].

Similar to Motif A, we propose that the cation partitioning selectivity in Motif B is also dictated by the competition between water coordination and favorable coordination with sulfonate groups. However, in contrast to Motif A, we propose that cation diffusivity in Motif B is not exclusively dictated by electrostatic interactions with sulfonate groups, but also influenced by interactions with water molecules and enhanced steric hindrance within the pore environment.

From Fig. 9, the coordination ratio in Motif B exhibits an increasing trend across different cations, which aligns with the observed partitioning behavior although Cs^+ partitioning is underestimated [Fig. 4(b)]. This overall agreement supports our hypothesis regarding the role of coordination competition in partitioning selectivity. The slight discrepancy observed for Cs^+ can be attributed to insufficient coordination in Motif B due to increased steric hindrance. Fig. S10 in the SI compares the number of coordinating water oxygen (O_w) and sulfonate oxygen (O_s) atoms between Motifs A and B. For Cs^+, the total coordination number of oxygen atoms is significantly reduced compared to other cations in Motif B. This is attributed to the larger bare ionic radius r_{bare} and correspondingly larger coordination shell of Cs^+, which enhances the steric exclusion effects on the shell. As a result, the substantial reduction in potential coordination leads to lower partitioning of Cs^+ than would be expected based solely on the degree of sulfonate coordination.

Additionally, in Motif B, the radial density peaks of Li^+ and Mg^{2+} ions are located further from the pore center compared to Na^+ and Cs^+, due to interactions with sulfonate groups positioned near the midpoint of the ligand chains. Steric hindrance from surrounding carbon atoms and the reduced mobility of sulfonate groups—now embedded in the backbone rather than at chain ends—limit the accessibility of these sites. As a result, Li^+ and Mg^{2+} ions form weaker interactions with sulfonate groups [Fig. 7(a)] and instead preferentially interact with water molecules [Fig. 7(b)]. This reduced sulfonate coordination relative to hydration (Fig. 9) leads to lower partitioning of these cations. The effect is particularly pronounced for Mg^{2+} due to its high charge density and originally strong interactions with sulfonate groups in Motif A.

The mechanisms governing diffusivity also change in Motif B. Unlike in Motif A, where cation–O_s RDFs were predictive of diffusivity trends, these interactions are weakened in Motif B and no longer explain the observed diffusivity order. Instead, the cation–O_w RDFs qualitatively align with the diffusivity trend, suggesting that hydration plays a more dominant role in mobility. Still, this alone does not explain the uniformly lower cation diffusivities observed in Motif B compared to Motif A. This reduction in mobility is attributed to structural changes in the pore environment: cations are displaced toward the pore wall [Fig. 8(b)], where steric hindrance is higher, and are exposed to reduced local water density due to the slightly larger ligand size and more crowded zwitterionic shell. These combined effects suppress ionic mobility across all cation species and account for why cation diffusivities in Motif B are consistently lower than that of Cl^-.

We note that differences in cation transport properties between the nanopores of Motif A and Motif B could also be influenced by the nanopore diameter and the grafting density of the ZIs. In our recent study,[27] we examined the impact of pore diameter on anion diffusivity within pores functionalized with ligand Motif A (e.g., effective radii of $r_{pore,eff}$ = 1.025 nm vs. 1.625 nm). Our results showed that, as the pore diameter increases, the density distribution of Na^+ shifts radially away from that of the sulfonate groups of the zwitterions. We hypothesize that this local spatial separation between Na^+ and the sulfonate groups leads to weakened Na^+—sulfonate interactions. Considering these findings, in Motif A, the density distributions of Mg^{2+}, Li^+, and Cs^+ are also expected to shift away from the sulfonate distribution with increasing pore size, resulting in weaker cation–sulfonate interactions. For Motif B, we similarly predict that increasing pore diameter will cause spatial separation between cations and sulfonate groups, thereby weakening their interactions with the sulfonate moieties of the ZI ligands. Consequently, the permselectivity for cations between Motif A and Motif B is expected to converge as the pore diameter increases.

Further, the same study[27] investigated the impact of reduced grafting density on anion diffusivity within pores functionalized with ligand Motif A [e.g., average separation between adjacent ZIs of l = 1.2 nm vs. 1.3 nm vs. ∞ (unfunctionalized pore)]. Our results revealed that in the unfunctionalized pore, the interaction between anions and water molecules weakens with increasing bare anion radius r_{bare} in the order: $F^- < Cl^- < Br^- < I^-$, leading to an increasing trend in anion diffusivities with bare anion radius r_{bare}. This tendency was counteracted by the presence of ligand Motif A: higher ZI grafting densities (l = 1.2 nm) promoted strong interactions between larger bare anions and the ammonium groups of ZI ligands, resulting in a decreasing trend of anion diffusivity with bare anion radius r_{bare}, whereas lower grafting densities (l = 1.3 nm) tended to preserve the diffusivity trend of the unfunctionalized nanopore.

Based on these previous findings, we hypothesize that in the case of Motif A, increasing the ZI grafting density would further reduce the diffusivity of Li^+ compared to Na^+ and Cs^+ due to stronger interactions with sulfonate groups. The partitioning of Li^+, however, would become stronger relative to Na^+ and Cs^+,

thereby maintaining the solution–diffusivity trade-off. In contrast, for the Motif B ligand, an increase in ZI grafting density is expected to enhance steric hindrance around sulfonate groups near the pore wall, making it more difficult for all cations to interact with these functional groups. As a result, while the diffusion selectivity among monovalent cations would remain unchanged, the partitioning selectivity would likely be reduced, leading to a reduction of overall cation permselectivity for Motif B.

In summary, structural differences between ligand motifs A and B lead to distinct ionic distributions and transport behaviors within the nanopores. In Motif A, sulfonate groups are concentrated near the pore center, resulting in strong electrostatic interactions with cations—especially Mg^{2+} and Li^+—that promote high partitioning but limit diffusivity. In contrast, Motif B exhibits a spatial shift of sulfonate groups toward the mid-region of the pore, leading to cation distributions skewed away from the center. For Mg^{2+} and Li^+, which prefer strong sulfonate coordination, this shift introduces steric constraints and weakens their interactions with sulfonates, enhancing hydration and lowering partitioning. Meanwhile, Na^+ and Cs^+—which inherently form weak sulfonate interactions—exhibit comparable interaction strengths across both motifs. These distinctions in interaction modes and density distributions underpin the divergent partitioning selectivities and transport properties observed. Specifically, in Motif A, Mg^{2+} and Li^+ overcome hydration due to strong sulfonate binding, resulting in high partitioning and low diffusivity. In Motif B, however, their interaction deficiencies and correspondingly lower sulfonate coordination reduce partitioning without significantly improving mobility, thus relatively favoring the selectivity and permselectivity of Na^+ and Cs^+ ions.

4 Conclusions

In this study, we employed molecular dynamics (MD) simulations to systematically investigate cation partitioning, diffusivity, and permselectivity in zwitterion (ZI)-functionalized nanopores bearing two distinct ligand architectures. These nanopore models differ in dipole orientation, denoted as Motifs A and B, and represent contrasting spatial organizations of the zwitterionic functional groups. Our goal was to elucidate how variations in dipole orientation and cation identity influence solubility, mobility, and overall transport behavior in ZI-grafted nanoconfined environments.

We first examined cation partitioning in ZI-functionalized nanopores by obtaining the PMF profiles for various cations through the nanopore. Our results revealed that cation partitioning behavior significantly differs depending on the difference in dipole orientation between Motifs A and B. In Motif A, Li^+ and Mg^{2+} ions showed high partitioning, reflecting energy barriers in the axial pore regions containing segments where $N_{H_2O}/N_{ZI-FGs} < 4$ (water-poor or ZI-rich). In contrast, for Motif B, Na^+ and Cs^+ partitioning is more prominent, resulting from cumulative energy barriers distributed across the entire pore.

Next, we proceeded to investigate cation diffusivities in zwitterion-functionalized nanopores. Our findings suggested that while both ligand motifs yield a trend of increasing cation diffusivity with bare ionic radius r_{bare}, Motif B shows lower self-diffusivities compared to Motif A consistently.

We then investigated cation permselectivity in functionalized nanopores based on the simulation results for their partitioning selectivity and self-diffusivities. Our results indicated that ion partitioning is the dominant factor governing cation permeability in this system. Particularly, Motif B showed a pronounced reduction in partitioning for both Li^+ and Mg^{2+}, with a more severe reduction for Mg^{2+}. This reduction leads to significantly higher permselectivity for Na^+ and Cs^+ over Mg^{2+} and Li^+, compared to X-ZAC membranes. Therefore, these results suggest that reversing dipole orientation within SBMA ligands in these membranes substantially improve monovalent cation selectivity.

Finally, we analyzed electrostatic interactions and spatial distributions of various cation chlorides in zwitterion-functionalized nanopores to rationalize cation transport properties (solubilities and diffusivities). Our results showed that in Motif A, sulfonate groups are concentrated near the radial center of the pore, leading to strong electrostatic interactions with Mg^{2+} and Li^+. This results in high partitioning but low diffusion following solution-diffusion tradeoff. In contrast, in Motif B, sulfonate groups shift toward the mid-region of the pore radially. This shift—particularly for Mg^{2+} and Li^+, which strongly prefer sulfonate coordination—introduces steric constraints and weakens their interactions with sulfonate groups, enhancing hydration and lowering partitioning while still maintaining low self-diffusivity. This hindered tradeoff explains enhanced selectivity among monovalent cations in Motif B (higher selectivity of Na^+ and Cs^+ over Li^+). Overall, our findings suggest that inverting the position of oppositely charged groups of ZI ligands in ZI copolymeric membranes can result in significant enhancement of the ion–ion separation efficiency. Specifically, positioning the negatively charged group of ZI ligands closer to the interface with the hydrophobic phase in the membranes is key to enhancing cation permselectivity in ZI copolymeric membranes. However, further experimental and computational studies involving various ZI chemistries are required to validate the generality of this hypothesis.

Author contributions

Kazuya Morishita: conceptualization, formal analysis, investigation, methodology, software, validation, visualization, writing – original draft, writing – review & editing. Harnoor Singh Sachar: conceptualization, methodology, software. Paul Irving: conceptualization, methodology. Nico Marioni: conceptualization, methodology. Majid Shahbabaei: conceptualization. Tyler J. Duncan: conceptualization. Zidan Zhang: conceptualization. Ying Zheng: conceptualization. Ashleigh Herrera: conceptualization. Nafiseh Khoshnevisan: conceptualization. Ayse Asatekin: funding acquisition, supervision, writing – review &

Conflicts of interest

There are no conflicts to declare.

Data availability

The datasets supporting the findings of this study are available in the SI. The SI includes details such as force field formulations and parameters used to reproduce the simulation results of the present study, the method to estimate permselectivity from experimental rejection results, the raw data used in the manuscript plots for partitioning selectivity, ion diffusivity, and permselectivity, as well as additional complementary analytical results. See DOI: https://doi.org/10.1039/d5sm00687b

The raw trajectory data from the molecular dynamics simulations are available from the corresponding author upon request.

Acknowledgements

Notes and references

1 D. Lu, Z. Yao, L. Jiao, M. Waheed, Z. Sun and L. Zhang, *Adv. Membr.*, 2022, **2**, 100032.

2 X. Li, Y. Mo, W. Qing, S. Shao, C. Y. Tang and J. Li, *J. Membr. Sci.*, 2019, **591**, 117317.

3 M. Jian, R. Qiu, Y. Xia, J. Lu, Y. Chen, Q. Gu, R. Liu, C. Hu, J. Qu, H. Wang and X. Zhang, *Sci. Adv.*, 2020, **6**, eaay3998.

4 R. Sujanani, M. R. Landsman, S. Jiao, J. D. Moon, M. S. Shell, D. F. Lawler, L. E. Katz and B. D. Freeman, *ACS Macro Lett.*, 2020, **9**, 1709–1717.

5 L. Kullman, M. Winterhalter and S. M. Bezrukov, *Biophys. J.*, 2002, **82**, 803–812.

6 T. Schirmer, *J. Struct. Biol.*, 1998, **121**, 101–109.

7 R. Koebnik, K. P. Locher and P. V. Gelder, *Mol. Microbiol.*, 2000, **37**, 239–253.

8 M. Roderick, *FEBS Lett.*, 2003, **555**, 62–65.

9 T. E. Webber, W.-G. Liu, S. P. Desai, C. C. Lu, D. G. Truhlar and R. L. Penn, *ACS Appl. Mater. Interfaces*, 2017, **9**, 39342–39346.

10 I. Sadeghi, P. Kaner and A. Asatekin, *Chem. Mater.*, 2018, **30**, 7328–7354.

11 S. J. Warnock, R. Sujanani, E. S. Zofchak, S. Zhao, T. J. Dilenschneider, K. G. Hanson, S. Mukherjee, V. Ganesan, B. D. Freeman, M. M. Abu-Omar and C. M. Bates, *Proc. Natl. Acad. Sci. U. S. A.*, 2021, **118**, e2022197118.

12 S. K. Lau and W. F. Yong, *ACS Appl. Polym. Mater.*, 2021, **3**, 4390–4412.

13 Y. Zhang, Y. Liu, B. Ren, D. Zhang, S. Xie, Y. Chang, J. Yang, J. Wu, L. Xu and J. Zheng, *J. Phys. D: Appl. Phys.*, 2019, **52**, 403001.

14 S. J. Lounder and A. Asatekin, *Proc. Natl. Acad. Sci. U. S. A.*, 2021, **118**, e2022198118.

15 S. J. Lounder and A. Asatekin, *Chem. Mater.*, 2021, **33**, 4408–4416.

16 G. Zhai, S. C. Toh, W. L. Tan, E. T. Kang, K. G. Neoh, C. C. Huang and D. J. Liaw, *Langmuir*, 2003, **19**, 7030–7037.

17 Q. Yang and M. Ulbricht, *Chem. Mater.*, 2012, **24**, 2943–2951.

18 C. Leng, X. Han, Q. Shao, Y. Zhu, Y. Li, S. Jiang and Z. Chen, *J. Phys. Chem. C*, 2014, **118**, 15840–15845.

19 S. Xiao, Y. Zhang, M. Shen, F. Chen, P. Fan, M. Zhong, B. Ren, J. Yang and J. Zheng, *Langmuir*, 2018, **34**, 97–105.

20 H. Huang, C. Zhang, R. Crisci, T. Lu, H.-C. Hung, M. S. J. Sajib, P. Sarker, J. Ma, T. Wei, S. Jiang and Z. Chen, *J. Am. Chem. Soc.*, 2021, **143**, 16786–16795.

21 H. Ohno, M. Yoshizawa-Fujita and Y. Kohno, *Phys. Chem. Chem. Phys.*, 2018, **20**, 10978–10991.

22 J. R. Keith and V. Ganesan, *J. Polym. Sci.*, 2020, **58**, 578–588.

23 Q. Shao and S. Jiang, *J. Phys. Chem. B*, 2014, **118**, 7630–7637.

24 P. Sarker, T. Lu, D. Liu, G. Wu, H. Chen, M. S. Jahan Sajib, S. Jiang, Z. Chen and T. Wei, *Chem. Sci.*, 2023, **14**, 7500–7511.

25 E. R. J. Nightingale, *J. Phys. Chem.*, 1959, **63**, 1381–1387.

26 H. S. Sachar, Z. Zhang, N. Marioni, E. S. Zofchak and V. Ganesan, *ACS Macro Lett.*, 2023, **12**, 1293–1297.

27 H. S. Sachar, E. S. Zofchak, N. Marioni, Z. Zhang and V. Ganesan, *Langmuir*, 2024, **40**, 9563–9578.

28 K. Morishita, H. S. Sachar, T. J. Duncan, Z. Zhang, N. Marioni, A. Herrera, A. Asatekin and V. Ganesan, *ACS Appl. Mater. Interfaces*, 2024, **16**, 57888–57900.

29 W. L. Jorgensen, D. S. Maxwell and J. Tirado-Rives, *J. Am. Chem. Soc.*, 1996, **118**, 11225–11236.

30 W. L. Jorgensen and J. Tirado-Rives, *Proc. Natl. Acad. Sci. U. S. A.*, 2005, **102**, 6665–6670.

31 J. L. F. Abascal and C. Vega, *J. Chem. Phys.*, 2005, **123**, 234505.

32 I. M. Zeron, J. L. F. Abascal and C. Vega, *J. Chem. Phys.*, 2019, **151**, 134504.

33 S. Blazquez, M. M. Conde, J. L. F. Abascal and C. Vega, *J. Chem. Phys.*, 2022, **156**, 044505.

34 W. G. Hoover, *Phys. Rev. A: At., Mol., Opt. Phys.*, 1985, **31**, 1695–1697.

35 S. Nosé, *J. Chem. Phys.*, 1984, **81**, 511–519.

36 I.-C. Yeh and G. Hummer, *J. Phys. Chem. B*, 2004, **108**, 15873–15879.

37 F. Zhu and G. Hummer, *J. Chem. Theory Comput.*, 2012, **8**, 3759–3768.

38 S. Kumar, J. M. Rosenberg, D. Bouzida, R. H. Swendsen and P. A. Kollman, *J. Comput. Chem.*, 1995, **16**, 1339–1350.

39 A. Grossfield, WHAM: The Weighted Histogram Analysis Method, **https://membrane.urmc.rochester.edu/wordpress/?page_id=126**, Accessed 2025, Version 2.1.0.

40 B. Roux, *Comput. Phys. Commun.*, 1995, **91**, 275–282.

41 G. M. Geise, D. R. Paul and B. D. Freeman, *Prog. Polym. Sci.*, 2014, **39**, 1–42.

42 H. Yasuda, C. E. Lamaze and L. D. Ikenberry, *Macromol. Chem. Phys.*, 1968, **118**, 19–35.

43 J. Wijmans and R. Baker, *J. Membr. Sci.*, 1995, **107**, 1–21.

44 G. Geise, B. Freeman and D. Paul, *Polymer*, 2010, **51**, 5815–5822.

45 Y. Marcus, *J. Chem. Soc., Faraday Trans.*, 1991, **87**, 2995–2999.

46 P. R. Irving, G. Sam, S. Rane, N. Thirumalai, N. Marioni, G. M. Geise, B. D. Freeman and V. Ganesan, *ACS Macro Lett.*, 2025, **14**, 161–168.

47 E. S. Zofchak, Z. Zhang, N. Marioni, T. J. Duncan, H. S. Sachar, A. Chamseddine, B. D. Freeman and V. Ganesan, *Macromolecules*, 2022, **55**, 2260–2270.

48 H. S. Sachar, E. S. Zofchak, N. Marioni, Z. Zhang, S. Kadulkar, T. J. Duncan, B. D. Freeman and V. Ganesan, *Macromolecules*, 2022, **55**, 4821–4831.

49 H. S. Sachar, N. Marioni, E. S. Zofchak and V. Ganesan, *Macromolecules*, 2023, **56**, 2194–2208.

50 L. M. Robeson, *J. Membr. Sci.*, 2008, **320**, 390–400.